A Protein-Based Janus Separator for Trapping Polysulfides and Regulating Ion Transport in Lithium–Sulfur Batteries

Min Chen,[a, b] Xuewei Fu,*[a] Jin Liu,[a] Zhiping Chen,[b] and Wei-Hong Zhong*[a]

Lithium–sulfur (Li–S) batteries are a promising candidate for the next-generation energy storage system, yet their commercialization is primarily hindered by polysulfide shuttling and uncontrollable Li dendrite growth. Here, a protein-based Janus separator was designed and fabricated for suppressing both the shuttle effect and dendrite growth, while facilitating the Li^+ transport. The Li metal-protecting layer was a protein/MoS_2 nanofabric with high ionic conductivity and good Li^+ affinity, thus capable of homogenizing the Li^+ flux and facilitating the Li^+ transport. The polysulfide-trapping layer was a conductive protein nanofabric enabling strong chemical/electrostatic interactions with polysulfides. Combination of the two layers was achieved by an integrated electrospinning method, yielding a robust and integral Janus separator. As a result, a long-lived symmetric Li|Li cell (>700 h) with stable cycling performance was demonstrated. More significantly, the resulting Li–S battery delivered greatly improved electrochemical performance, including excellent rate capacity and remarkable cycle stability (with a low decay rate of 0.063% per cycle at 0.5 A g^{-1} over 500 cycles). This study demonstrates the effectiveness of the Janus separator configurations for simultaneously addressing the shuttle effect and dendrite growth issues of Li–S batteries and broadens the applications of electrospinning in electrochemistry community.

Introduction

The growing development of various electronic devices and electric vehicles spurs the demand for energy storage devices with higher energy density. Lithium–sulfur (Li–S) batteries employing eco-friendly and cost-effective sulfur as the cathode have attracted extensive attention due to their high theoretical specific capacity (1673 mAh g^{-1}) and high energy density (2600 Wh kg^{-1}).[1] However, the practical application of Li–S batteries is plagued by two significant hurdles: (i) the shuttle effect, which is caused by the intermediates of sulfur reduction that can dissolve into the electrolyte and diffuse to the anode side, leading to irreversible loss of active material sulfur and anode corrosion;[2] (ii) Li dendrite growth, coupled with unstable solid electrolyte interphase (SEI) layer, which results in electrolyte consumption, "dead Li" formation, and even separator piercing.[3] These two critical problems will deteriorate battery performance and increase safety hazards; thus, simultaneously solving them becomes the foremost task to commercialize Li–S batteries.

To effectively overcome the shuttle effect, core-shell cathode structures,[4] polysulfide-philic binders,[5] solid or gel electrolytes with limited solubilities of polysulfides,[6] polysulfide-blocking separator coatings,[7] and other methods have been applied. As for suppressing the Li dendrites, considerable attention has been paid to using electrolyte additives,[8] decorating separators,[9] and constructing artificial protection layers[10] and 3D host materials.[11] These remedies have achieved great success and rational combination of them is expected to solve the two issues in a Li–S battery. However, there is always a need for seeking facile strategies, and avoiding multicomponent modifications is hence necessary. Separators are in direct contact with both electrodes via interfaces and play a key role in mass/ion transport. Therefore, functionalization of separators is among the most facile and simplified strategies, enables the interface engineering toward both electrodes, and is adaptable in existing battery production flow.

The separator decorating materials for suppressing the shuttle effect are mainly nanostructured carbon materials[12] and polysulfide-trapping substances [e.g., metal oxide/metal nitride heterostructure, conductive metal-organic frameworks (MOFs), polar polymers],[13] which can physically block, chemically adsorb, or electrostatically adsorb/reject the polysulfides. In contrast, for suppressing the Li dendrites, ceramic particles (Al_2O_3,[14] SiO_2,[9a] TiO_2,[15] etc.), metals (Cu,[16] Mg,[9b] etc.), and polymers[17] are important modifiers for increasing mechanical strength, reducing effective current density, or killing dendrites by reacting with Li. Adding functional layers on both sides of the separator, thus, has the potential to simultaneously suppress the shuttle effect and dendrite growth. For example, a Janus separator with ammonium alcohol polyvinyl phosphate/carbon black (AAPP/CB) and $Li_{1.5}Al_{0.5}Ge_{1.5}(PO_4)_3$ (LAGP) covered on each side of the polypropylene (PP) separator was reported recently.[18] Even though dual-sided modification of separators has been widely reported and significant progress has been made,[19] the applied functional layers result in extra ion-transport distance, which lowers the ion-transport kinetics, rate

[a] Dr. M. Chen, Dr. X. Fu, Prof. J. Liu, Prof. W.-H. Zhong
School of Mechanical and Materials Engineering
Washington State University
Pullman, WA 99164 (USA)
E-mail: xuewei.fu@wsu.edu
Katie_zhong@wsu.edu
[b] Dr. M. Chen, Dr. Z. Chen
College of Materials Science and Engineering
Chongqing University
174 Shazhengjie, Chongqing, 400044 (P. R. China)

Supporting information for this article is available on the WWW under https://doi.org/10.1002/cssc.202100568

performance, and overall energy density of the batteries. Therefore, designing and fabricating a Janus separator with two tailored functional components, instead of introducing two layers on a conventional separator, is urgently demanded to achieve safe and stable Li–S batteries with high energy density.

Our previous study[20] indicated that proteins with a proper molecular structure, particularly short-branched proteins, offer stronger interactions with polysulfides than long-branched proteins and conventional polar polymers such as polyvinylpyrrolidone (PVP). More significantly, the rich functional groups of proteins provide unique interactions with Li^+ and counterions,[21] which leads to the potential to increase the Li-ion transference number, such that the formation of Li dendrites can be suppressed.[22] Based on the significant findings, in the current work, we design and fabricate a Janus separator derived from the short sidechain-dominated protein, gelatin, to combine the functions of trapping polysulfides, facilitating Li^+ transport, and stabilizing Li^+ deposition. Specifically, the cathode-facing layer is a conductive protein nanofabric that can effectively trap and convert polysulfides, while the anode-facing layer is a composite gelatin/MoS_2 nanofabric that regulates the Li^+ flux distribution and enables uniform Li^+ deposition. As a result, our Janus separator significantly improves the electrochemical performance of Li–S batteries, including superior rate performance (757 mAh g^{-1} at a current density of 1 A g^{-1}) and excellent cycle stability (with a capacity fade rate of 0.063% per cycle at 0.5 A g^{-1} over 500 cycles).

Results and Discussion

To design and fabricate a Janus separator with integrating the functions of trapping polysulfides, stabilizing Li metal while facilitating the transport of Li^+, we propose an asymmetric configuration consisting of two protein-based functional nanofabrics (NFs) in parallel. Gelatin protein plays three important roles in this study: (i) as a polysulfide-philic agent, (ii) as a Li-stabilizing agent, (iii) and as an exfoliation agent for MoS_2. These unique features lead to a multifunctional Janus separator that can effectively improve the battery performance. As shown in Figure 1a, the layer facing the S-cathode is an electrospun gelatin NF compositing with conductive agents, while the layer toward the Li-anode is a composite gelatin/MoS_2 NF. Combination of the two functional layers is realized via a facile integrated electrospinning method, in which the gelatin/MoS_2 NF is directly deposited on the surface of conductive gelatin NF via electrospinning. The generated Janus separator incorporates the respective advantages of both gelatin-based NFs: the conductive gelatin NF enables the trapping-conversion of polysulfides; the gelatin/MoS_2 NF with high Li^+ affinity and ionic conductivity allows the fast Li^+-transport and stable ion

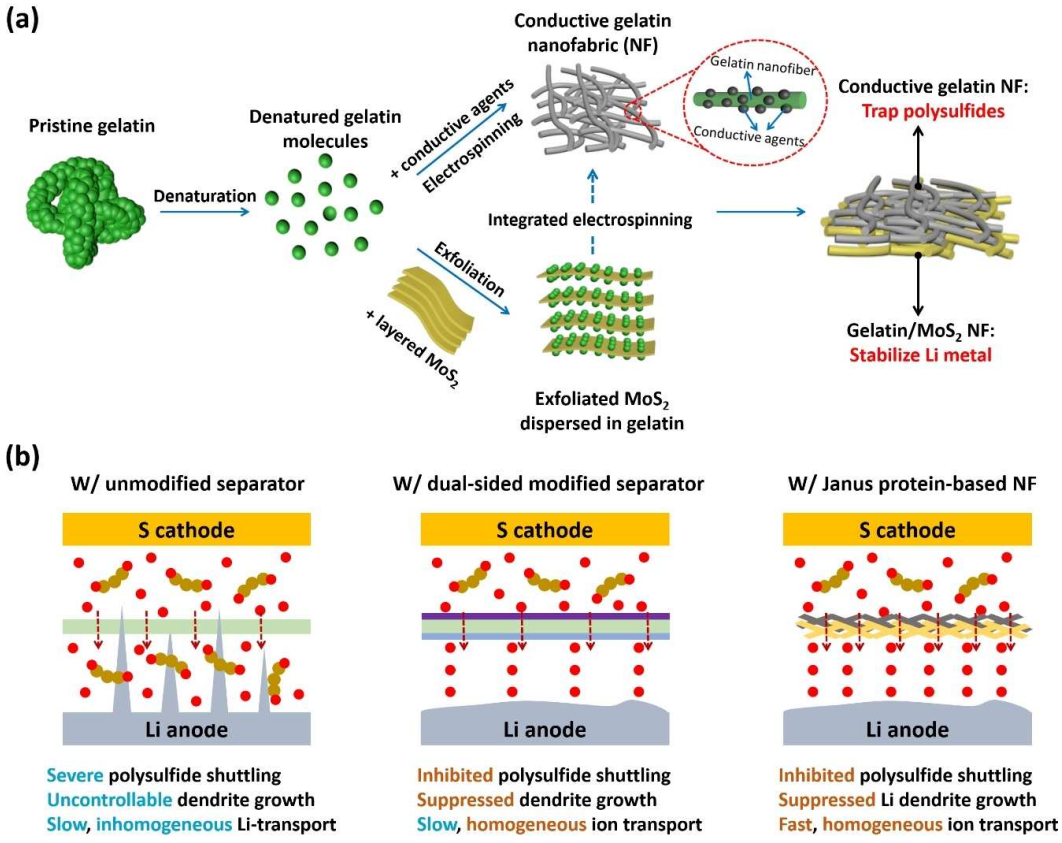

Figure 1. Schematic illustration of Janus protein-based NFs for Li–S batteries. (a) Fabrication of the Janus protein-based NFs via an integrated electrospinning method. (b) Comparison of the polysulfide shuttling and Li dendrite growth situations with different separators.

deposition. Meanwhile, the nanofibrous structure of the Janus separator and rich polar groups (e.g., –OH, –COOH, $–NH_2$, etc.) from gelatin[23] lead to high electrolyte uptake, which ensures the generation of numerous ion-conduction pathways. The integrated electrospinning method yields a stronger adhesion between two layers than simply compressing them, such that sufficient mechanical flexibility and structural integrity are assured, bringing about good processability and compatibility with current battery production.

As illustrated in Figure 1b, compared with an unmodified separator or a conventionally dual-sided modified separator, our protein-based Janus separator brings in the benefits of inhibition of both shuttle effect and dendrite growth, and facilitation of Li^+ transport. Unmodified nanoporous separators fail to suppress the crossover of polysulfides and the growth of Li dendrites due to the nonhomogeneous deposition of Li^+. Modifying both surfaces of the separator can stabilize the interfaces for both electrodes: inserting a cathode-facing layer that can block the polysulfide diffusion and an anode-facing layer that can homogenize the Li^+ flux is able to solve the shuttle effect and dendrite growth issues. However, this modification strategy notably increases the thickness or the ion-transport distance, which sacrifices the ion-transport kinetics. Our proposed Janus separator can effectively address this critical hurdle, in addition to suppressing the polysulfide crossover and homogenizing Li^+ flux, benefiting from its unique structures and functions as discussed above.

MoS_2 is a Li^+-conducting layered material,[24] such that incorporating it with the Li-anode facing layer is expected to further promote the transport of Li^+. However, nanosheets of bulk MoS_2 are bound together by van der Waals forces. The various kinds of functional groups of proteins including polar and nonpolar groups enable an effective exfoliation of stacked and aggregated nanomaterials such as graphitic nanaplatelets (GNPs),[25] carbon nanotubes (CNTs),[26] graphene oxide (GO),[27] and others. In this work we apply gelatin to exfoliate bulk MoS_2 into few- or mono-layer thin sheets. Figure 2a shows the process for exfoliating bulk MoS_2 using gelatin as the surfactant and stabilizer. Gelatin can adhere to the nanosheet surface via hydrophobic-hydrophobic interactions due to the nonpolar groups such as aromatic residues. In this scenario, the restacking of MoS_2 nanosheets is prevented by the adsorbed gelatin, and meanwhile the outside polar groups assist the dispersion stability. Figure 2b compares the stability of MoS_2 dispersions having been sonicated with or without gelatin. Both of the as-prepared MoS_2 dispersions are uniform. The color of MoS_2/gelatin dispersion is dark green and that of pure MoS_2 is black, which means that MoS_2 is well-dispersed in gelatin solution. After for 2 days, there is an obvious precipitation in MoS_2 dispersion while the MoS_2/gelatin is still stable and uniform.

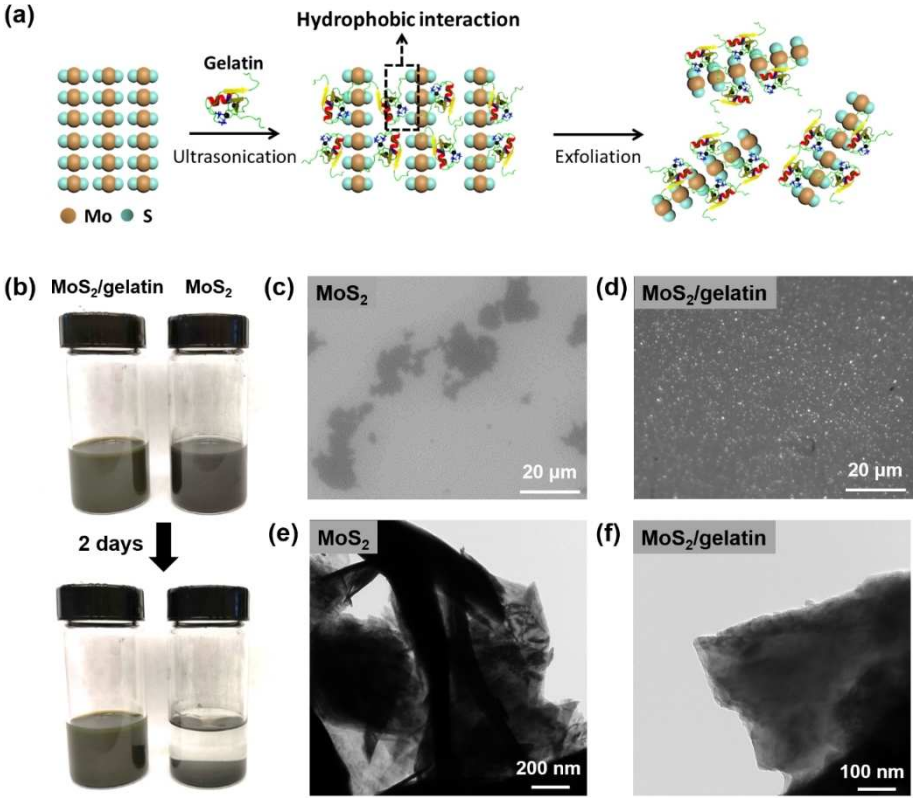

Figure 2. Contribution from gelatin on exfoliation and dispersion stability of MoS_2. (a) Schematic illustration of the exfoliation process of MoS_2 by gelatin. (b) Digital photos of the stability of MoS_2 and MoS_2/gelatin dispersions. (c, d) Optical microscopic images of MoS_2 dispersions with or without gelatin. (e, f) TEM images of MoS_2 dispersions with or without gelatin.

To further analyze the dispersion quality, the optical microscopic images were taken and shown in Figure 2c,d. In the pure MoS_2 dispersion (Figure 2c), the aggregation phenomenon is obvious and MoS_2 tends to aggregate into particles larger than 20 μm (Figure S1 in the Supporting Information). In sharp contrast, exfoliated with the aid of gelatin, the particle size is highly reduced, and MoS_2 particles can be hardly observed due to the extremely small size (Figure 2d). From the transmission electron microscopy (TEM) results (Figure 2e,f), one can see the overlapping of MoS_2 nanosheets in the pure MoS_2 dispersion, while the flakes are thinner in MoS_2/gelatin. These results indicate that gelatin can help exfoliate and disperse MoS_2 nanosheets, and the adsorbed gelatin on the surface prevents them from re-aggregation, thus improving the dispersion stability.[28]

After the MoS_2 was exfoliated in gelatin solution, it was centrifuged, and the upper stable dispersion was mixed with a 25 wt% gelatin solution to increase the viscosity for electrospinning. The scanning electron microscopy (SEM) image of the obtained gelatin/MoS_2 NF can be seen in Figure 3a, and the inset is the corresponding TEM image. Both gelatin and gelatin/MoS_2 NFs show an interconnected nanofibrous structure (see more SEM images in Figure S2). As shown in Figure S3 the gelatin/MoS_2 NF exhibits an average fiber diameter of 145 nm with a concentrated distribution, which is slightly higher than that of pure gelatin NF (112 nm). From the TEM result in Figure 3a, no MoS_2 particles can be observed because of the low loading (≈0.1 wt%) and extremely thin MoS_2 nanosheets. Although this finding is "seemingly" inconsistent with the TEM image from Figure 2f showing restacking of MoS_2 nanosheets to some extent, the result in Figure 3a is closer to the realistic dispersion quality of MoS_2. The solvent removal process for TEM observation possibly led to the reaggregation of MoS_2; while for preparation of gelatin/MoS_2 NF, the dispersion state of MoS_2 in solution was maintained until the NF was electrospun.

Fast ion-conduction is a key enabler to achieve high rate-capability of batteries. The ionic conductivity of the two gelatin-based NFs is compared in Figure 3b. Both NFs show higher ionic conductivity than that of a commercial separator (0.6 mS cm^{-1}).[22] The improved ionic conductivity benefits from the nanofibrous structure allowing higher electrolyte uptake and more ion-conduction pathways, and the polar groups of gelatin that increase the Li^+ affinity.[21] Significantly, the gelatin/MoS_2 NF shows a further increased ionic conductivity (5.5 mS cm^{-1}) compared with gelatin NF (4.6 mS cm^{-1}), due to the presence of Li-conductive MoS_2.[29] In addition, we studied the wettability of the NFs with liquid electrolytes using contact angle measurement. The commercial separator shows a poor wettability with the liquid electrolyte and the contact angle is 56.8° (Figure S4). On the contrary, both gelatin and gelatin/MoS_2 NFs present remarkable wettability with the electrolyte. As shown the electrolyte droplets promptly infiltrate the NFs and are completely absorbed by the NFs, gradually, leading to a finial contact angle of 0° after 15 s (Figure 3c). The improved ionic conductivity and excellent wetting behavior of the liquid electrolyte are synergistically contributed by the nanofibrous structure and surface polarity of gelatin.

To investigate the contribution from the gelatin-based NFs on the Li^+ deposition process, we carried out Li plating/stripping test using Li|Li cells with different separators. As shown by the voltage profile in Figure 4a, under a current density of 0.5 mA cm^{-2} (1 h for each plating or stripping period with an areal capacity of 0.5 mAh cm^{-2}), the overpotential of the cell with commercial Celgard® separator is much higher than that of the two cells with gelatin and gelatin/MoS_2 NFs. After cycling for 100 h, the cell with a commercial separator encounters a huge increase in polarization resulting from the inhomogeneous and unstable Li^+ deposition, which induces the excessive formation of Li dendrites and "dead" Li on the surface of Li metal. In contract, the cells with gelatin and gelatin/MoS_2 NFs deliver much smaller and more stable overpotential and ultralong cycle life for more than 700 h This result indicates that the gelatin-based NFs present lower energy barrier for the nucleation and striping of Li. Notably, in Figure 4b the gelatin/MoS_2 NF generates lower overpotentials compared with that of gelatin NF (see the magnified voltage profiles in Figure S5). This is attributed to the improved ionic conductivity of gelatin/MoS_2 NF, which facilitates the ion-transfer as revealed above.

The interfacial stability of the symmetric cells was investigated by electrochemical impedance measurement to monitor the growth of SEI layer. The Nyquist plots of symmetrical cells at 5 and 15 cycles are shown in Figure 4c,d. The interfacial resistance between electrolyte/anode surface is associated with the semi-circle in the high-frequency region.[30] After 5 cycles of Li plating/striping process, the Celgard® cell shows a high

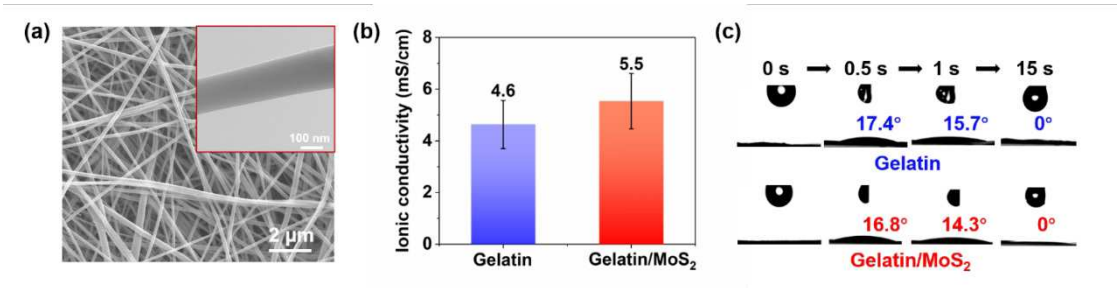

Figure 3. Ionic conductivity and wettability comparation of gelatin and gelatin/MoS_2 NFs. (a) SEM image of gelatin/MoS_2 NF. The inset is the TEM image. (b) Ionic conductivity comparison. (c) Evolution of contact angles with the time.

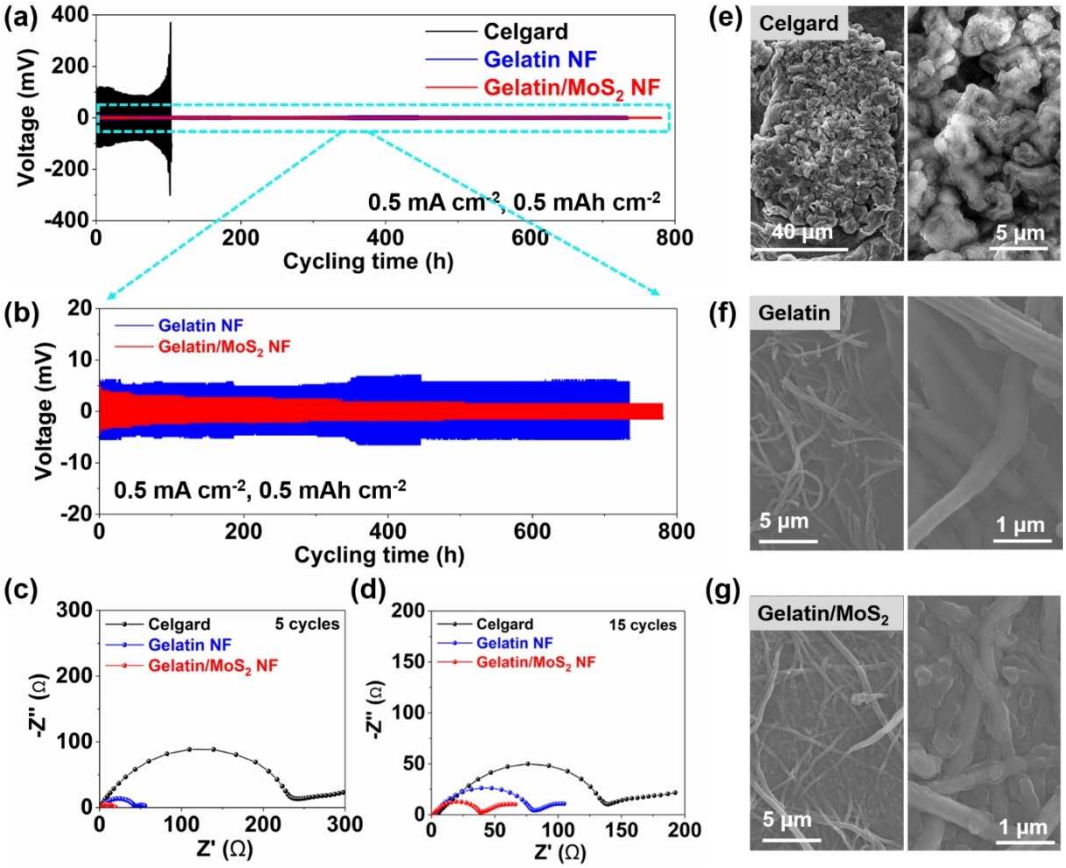

Figure 4. Li plating/striping behaviors. (a, b) Voltage profiles of symmetric Li | Li cells at a current rate of 0.5 mA cm^{-2} with different separators. (c, d) Nyquist plots of the symmetric cells after 5 and 15 cycles, respectively. (e–g) SEM images of cycled Li metals from cells with different separators.

interfacial resistance of about 236 Ω due to the formation of thick SEI film on the Li anode. The gelatin NF and gelatin/MoS_2 NF show much smaller interfacial resistances of 40 and 15 Ω, respectively. This result suggests that the nanofibrous structure accelerates the charge transfer process, benefiting from the increased ionic conductivity. Additionally, after 15 cycles, the interfacial resistance of the cell with a commercial separator is still the highest among the three cells, although it decreases to144 Ω, which results from the breaking of the original and unstable SEI film allowing exposure of fresh Li. The resistances of gelatin NF and gelatin/MoS_2 NF increase to 77 and 37 Ω, respectively, suggesting the gradual generation of SEI film. From the long-term cycling (Figure 4a,b), the stable voltage profile of gelatin/MoS_2 cell indicates the thin and uniform SEI film formation after many cycles. In contrast, the Celgard® cell encounters severe Li dendrite growth and successive electrolyte consumption, leading to continuous SEI formation and increased polarization.

In the ex-situ SEM analysis after Li plating/stripping cycling, the cycled Li anode with a commercial separator shows an extremely rough and porous structure, as shown in Figure 4e. The nonuniform deposition of Li is amplified as the cell being cycled, eventually becoming Li dendrites that penetrate the separator. By contrast, the Li anodes disassembled from the cells with gelatin or gelatin/MoS_2 NFs are much smoother and dendrite-free (Figure 4f,g). The morphology improvement is attributed to the steady or uniform ion deposition that diminishes the nucleation of Li dendrites.[31] It is also seen that Li metals fill the free spaces of the NFs yielding a smooth film-like structure, which indicates excellent affinity between the NFs and Li. This is because the rich polar groups of gelatin (e.g., –OH group) generate good affinity with Li^+ and electrolytes, which is consistent with a significant number of studies[32] that used biomaterials to homogenize Li^+ flux. The 3D structure and high specific surface area of the NFs help lower the local current density against the anode surface, which reduces the "tip effect"[33] and further suppresses the formation of Li dendrites. At the same time, the good Li^+ affinity from both the gelatin and MoS_2 deeply benefits the fast ion-transfer.

The cathode-facing layer to curtail the shuttle effect is a conductive gelatin NF made of gelatin and conductive agents (carbon black and carbon nanofiber). As shown in Figure 5a, the conductive gelatin NF shows a nanofibrous structure and carbon black (CB) particles are obviously embedded inside the fibers. From the TEM image in Figure 5b, we can see hollow CNFs inside a single fiber, which helps the formation of continuous electronic-conduction pathways. CB particles surrounding around the CNF increase the surface area of the NFs,

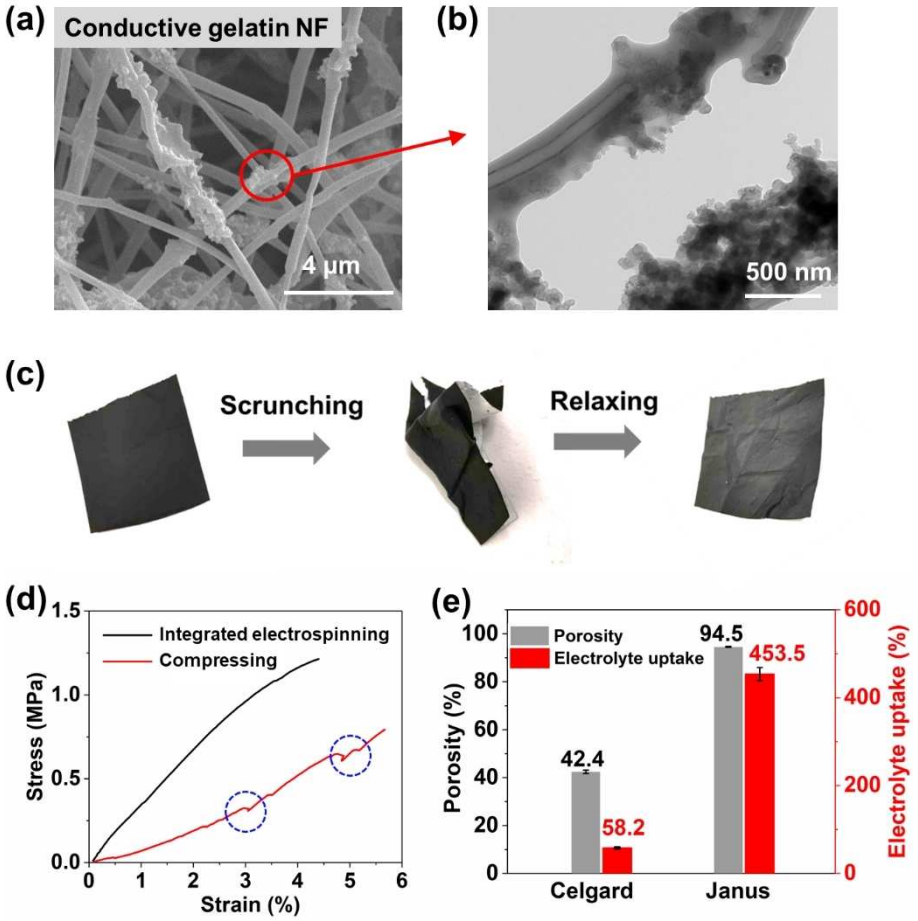

Figure 5. Morphology, mechanical properties and porous structure of the Janus separator. (a) SEM and (b) TEM images of conductive gelatin NF. (c) Photographs of the flexible Janus separator. (d) Tensile stress-strain curves of integrated Janus separator and compressed two layers (conductive gelatin NF and gelatin/MoS_2 NF). (e) Porosity and electrolyte uptake of Celgard® and Janus separators.

providing more active sites for trapping and converting polysulfides. Mechanical properties of electrospun nanofibers are often weak because of their thin fiber diameters. We find that our Janus separator shows a good mechanical flexibility after undergoing severe deformation, and importantly, the integrated electrospinning method generates good structural integrity of the two NF layers. As shown in Figure 5c the Janus separator can withstand harsh scrunching and no crack or delamination is observed after relaxing. To further explore the advantage of the integrated electrospinning method, we compare the tensile performance of the Janus separator fabricated by simply compressing the two layers of gelatin/MoS_2 NF and conductive gelatin NF. The stress-strain curves can be seen in Figure 5d. Basically the integrated Janus separator shows a significantly higher Young's modulus than that of the Janus separator via compressing method (see Figure S6). Meanwhile, the Janus separator fabricated by integrated electrospinning shows a continuously stable stress increase, which indicates a good structural integrity. However, the counterpart via compressing two layers shows a fluctuated stress-strain curve even with two obvious stress drops at strains of approximately 3 and 5%, which result from the delamination and breaking of two individual layers. This result indicates that the integrated electrospinning leads to a higher interfacial adhesion between the two layers due to the strong protein-protein interaction during the fiber deposition process. In addition, the porosity and electrolyte uptake of the Janus separator are 94.5 and 453.5%, respectively, both of which are much higher than that of a commercial separator (Figure 5e). This is beneficial for providing sufficient ion-conduction pathways and fast ion-transfer.

Electrochemical impedance spectroscopy (EIS) for the fresh cells with different separators at discharging status were performed with a frequency range of 0.01–1 MHz. Typical EIS plots with equivalent circuit models are shown in Figure 6a,b and the fitting results of electrochemical impedance parameters are summarized in Table S1. The Nyquist plot shown in the intercept on the real axis at high frequency corresponds to the ohmic resistance (R_b) resulting from the electrolyte resistance, current collectors, and cell contributions. The high-to-medium frequency region is fitted with two parallel connections of R and CPE, relating to the charge transfer process (R_{CT}//CPE_{CT}) and the interface impedance (R_{SEI}//CPE_{SEI}), respectively. The low-frequency region is a diffusion-related process and is simulated

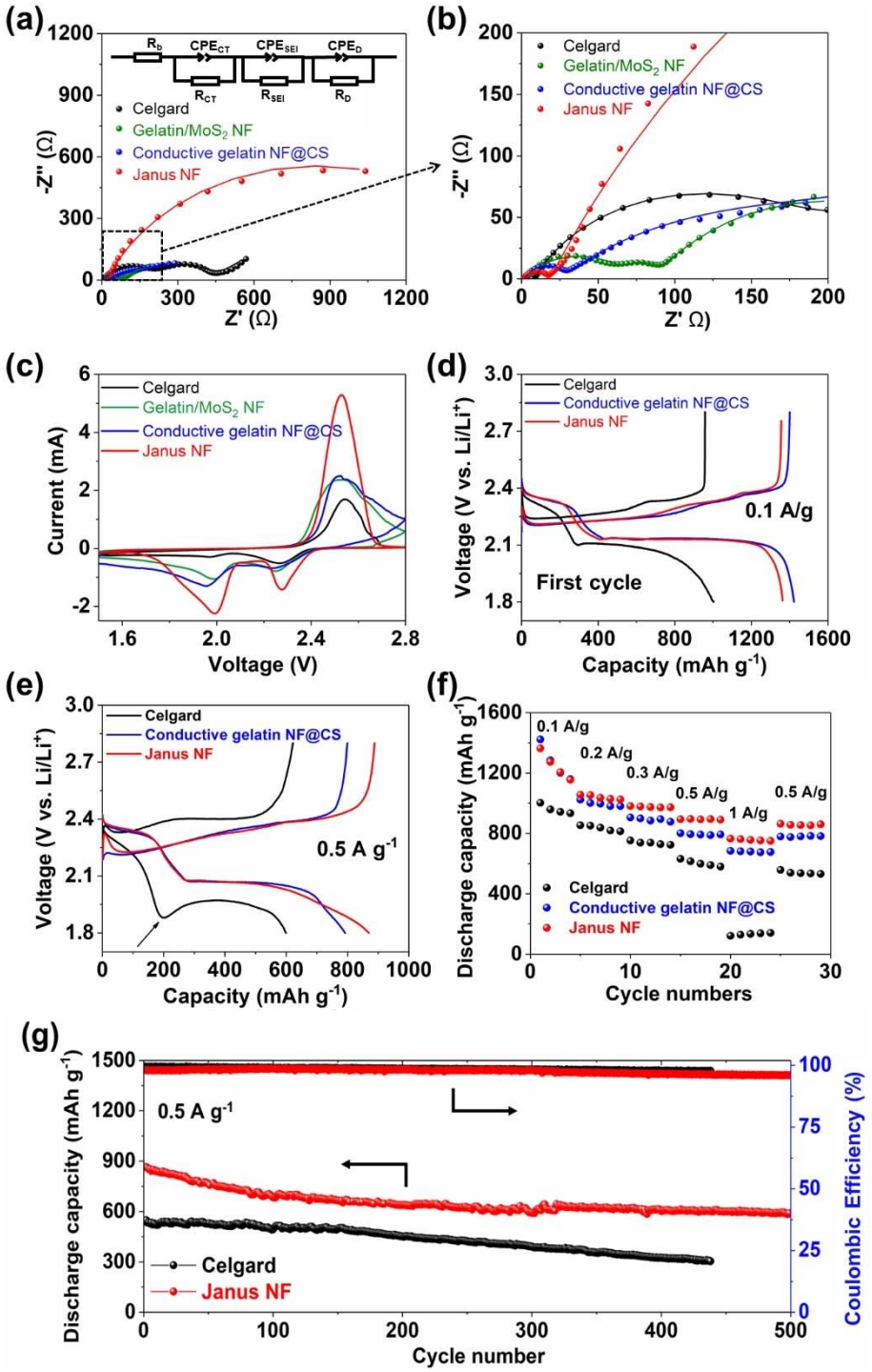

Figure 6. Electrochemical performance of Li–S batteries with Janus separator compared with its counterparts. (a, b) Electrochemical impedance spectra of fresh Li–S batteries with different separators at discharge status over a frequency range of 0.01–1 MHz. The solid lines indicate the fitting results. (c) CV curves of Li–S batteries with different separator at a scan rate of 0.1 mV s^{-1}. Charge-discharge profiles of Li–S batteries at (d) 0.1 A g^{-1} and (e) 0.5 A g^{-1}. (f) Rate performance of Li–S batteries. (g) Cycle performance of Li–S batteries at a current density of 0.5 A g^{-1}.

by R_D//CPE_D.[34] Generally the three NFs show lower charge transfer resistances (R_{CT}) than that of the Celgard® separator, due to the higher ionic conductivity. More specifically, the Janus separator exhibits the lowest R_{CT} (17.2 Ω) among the three NFs, because of the combined effect from the improved electrical/ionic conductivity by the two NF layers. The interface resistance indicates the Li-ion diffusion resistance through the Li_2S/Li_2S_2 solid film. For the two cells containing the conductive gelatin NF, that is, conductive gelatin NF with commercial separator (conductive gelatin NF@CS) and Janus separator, the R_{SEI} can be

ignored, suggesting the strong polysulfide-trapping capability of the conductive gelatin NF. When applying the gelatin/MoS_2 NF as a separator, the R_{SEI} (17.2 Ω) is much smaller than that of Celgard® (227.8 Ω), because both gelatin and MoS_2 have been demonstrated to have interactions with polysulfides.[7a,35] The EIS results reveal that the Janus separator presents the capabilities of trapping polysulfides and facilitating the charge-transfer process.

Figure 6c shows the cyclic voltammetry (CV) curves of the coin cells with different separators in the potential range of 1.5–2.8 V with a scanning rate of 0.1 mV s^{-1}. The two cathodic peaks correspond to the conversion of cyclo-S_8 to soluble long-chain polysulfides (Li_2S_n, $4 \leq n \leq 8$) and then further reduction to short-chain polysulfides (Li_2S_n, $1 \leq n \leq 4$). Specifically, the cell with the Janus separator shows higher reduction peaks and a lower oxidation peak when compared with the other three cells. The minimum polarization voltage (ΔE) indicates that the existence of the Janus separator accelerates the electrochemical process. The individual anodic peak is associated with the reversible transformation of Li_2S_2/Li_2S to S_8. The cell with the Janus separator displays well-defined redox peaks with higher peak currents, suggesting a rapid conversion kinetics, which benefits from the excellent conductivity of the conductive gelatin NF. The larger area also demonstrates a higher utilization of active sulfur due to the strong adsorption of polysulfides.

The improved active material utilization and low polarization of the cell with the Janus separator are further confirmed by a comparison of the discharge/charge curves of cells with different separators at a current density of 0.1 and 0.5 A g^{-1} (Figure 6d,e). The three cells all exhibit typical two plateaus during discharging and one plateau during charging process, which are consistent with the CV results. At a small current density of 0.1 A g^{-1}, the cells with Janus NF or conductive gelatin NF@CS separator exhibits similar voltage hysteresis that is smaller than the Celgard® cell. The capacities of the two cells (1423 and 1363 mAh g^{-1}, respectively) are much higher than that of Celgard® cell (1002 mAh g^{-1}), suggesting that the effective trapping and conversion of polysulfides is due to the polar-polar and electrostatic interactions between gelatin and polysulfides revealed by our previous work.[5b,36] At a high current density of 0.5 A g^{-1}, the Celgard® cell shows severe polarization with a high voltage hysteresis. The voltage of discharge shows an obvious peak, as indicated by an arrow in Figure 6e, which suggests that the electrolyte has high viscosity as a combined result of the S–S chain length and the number of polysulfide anions.[37] As for the cell with Janus separator, the soluble Li_2S_4 can be absorbed by the separator and then reduced to insoluble Li_2S_2/Li_2S at high rate, thus no similar peak is observed at the discharge curve. The discharge capacity of cell with Janus separator keeps its advantage and remains to be 908 mAh g^{-1}, which is higher than that of conductive gelatin NF@CS. This suggests that the gelatin/MoS_2 NF can further anchor the polysulfides that escape from the conductive gelatin NF@CS and improve the capacity. However, it is noted that the areal density of the Janus separator is approximately 1.41 mg cm^{-2} (carbon content: 29 wt%), higher than that of a commercial separator (0.85 mg cm^{-2}), due to the presence of carbon materials. If we consider the carbon materials from the Janus separator, the actual sulfur content is reduced from 63.8 to 54.5 wt%. To build a high-energy-density Li–S battery, it is necessary to further increase the S loading and reduce the thickness/carbon loading of the Janus separator. Via optimization of the cathode structure, the dispersion quality of carbon materials and the fiber morphologies, it is expected to push forward the progress to achieve that goal.

The rate performance of Li–S cells was tested from a current density of 0.1 to 1 A g^{-1}. As shown in Figure 6f, the cell with the Janus separator achieves superior rate performance than the counterparts, which delivers average discharge capacities of 1250, 1040, 976, 894, and 757 mAh g^{-1} at different current densities of 0.1, 0.2, 0.3, 0.5, and 1 A g^{-1}, respectively. When the current density is recovered to 0.5 A g^{-1}, a capacity of 858 mAh g^{-1} (with a retention of 96.0%) is maintained, demonstrating the outstanding structure stability of the Janus separator and the accelerated charge-transfer process. In contrast, the cell with a pristine separator shows much lower capacities at all current densities due to the severe shuttling effect of polysulfides. The cell suffers from a significant capacity decay to 132 mAh g^{-1} at 1 A g^{-1}, implying limited charge transfer pathways that slow down the Li^+ diffusion and lead to high polarization. The cycle performance of Li–S batteries with the Janus separator was evaluated at 0.5 A g^{-1} (Figure 6g). The cell shows an initial discharge capacity of 865.6 mAh g^{-1} and the capacity remains 593.5 mAh g^{-1} after 500 cycles with a low decay rate of 0.063% per cycle. As for the cell with a Celgard® separator, the initial capacity is 540 mAh g^{-1} and decays to 325 mAh g^{-1} after 400 cycles due to a substantial loss of sulfur active materials resulting from the severe shuttle effect. The overall capacity of the Janus cell is much higher than that of the Celgard® cell, showing the advantage of the Janus NF as a separator in Li–S batteries. The slightly inferior efficiency of the Janus separator can be explained from two aspects. On one hand, this phenomenon indicates that the diffusion of polysulfides is mitigated at the beginning, but some diffusion occurs gradually over cycling, leading to reduced efficiency. In contrast, for the cell with a commercial separator, the diffusion and consumption of sulfur occur promptly in the first several cycles, generating considerable sacrificed sulfur species. This is why the capacity is significantly decayed. However, higher coulombic efficiencies can be achieved because the battery environment reaches the final equilibrium state soon. On the other hand, the large pores of the Janus separator may result in sulfur loss to some extent, which is anticipated to be solved via morphology modification by optimizing fabrication process.

We further tested the Li–S cells using a high-sulfur-loading (4.3 mg cm^{-2}) cathode and thin lithium anode (thickness: 50 μm). Meanwhile, we reduced the area of lithium anode to 1.27 cm^2, which is the same as that of sulfur cathode. The results in Figure S7 show that the Janus separator delivers much higher capacities (> 850 mAh g^{-1}) and more stable voltage profiles compared with the commercial separator presenting a capacity < 600 mAh g^{-1}. Although the results obtained thus far demonstrate the advantage and potential of

the Janus separator to be applied in high loading Li–S batteries, more in-depth studies are necessary to prolong the cycle life and increase the capacity.

To further reveal the Li metal-protecting and polysulfide-trapping capabilities of the Janus separator, the cycled Li–S batteries were disassembled to observe the Li anode and the Janus separator. Figure 7a,b shows the morphologies of Li metal disassembled from Li–S batteries with Celgard® or Janus separators. The Li metal with the Celgard® separator shows many cracks on the surface, due to the severe corrosion by polysulfides. On the contrary, for the Li metal from the cell with Janus separator, Li deposits along with the fibers and embeds with the voids among the fibers gradually, which finally generates a film-like surface. This result supports that the Janus separator can regulate the deposition of Li^+ and inhibit the Li dendrite growth. The two sides of the cycled Janus separator were observed with SEM as shown in Figure 7c,d. In Figure 7c, a large number of sulfur-related substances are blocked by the conductive gelatin NF, which greatly restrains the shuttle effects. On the other side of the Janus separator, the gelatin/MoS_2 NF basically maintains its fibrous structure and some polysulfides are adsorbed on the fiber surface, which further guarantees the polysulfide-trapping effects of the Janus separator. Meanwhile, the retentive fibrous structure provides fast Li^+-diffusion pathways, thus improving the rate performance. Diffusion experiment was conducted to visualize the trapping capability of the Janus separator. As shown in Figure 7f, yellow Li_2S_6 solutions [in 1,3-dioxolane/1,2-dimethoxyethane (DOL/DME)] are separated from the pure DOL/DME by Celgard® (left) or Janus separator (right). An obvious diffusion of the polysulfides is observed in the case of Celgard® as time elapses, as the solution color at the bottom changes from colorless to yellow and then to brown yellow after 80 h. However, almost all the polysulfides are absorbed by the Janus separator, suggested by the fact that the solution at the bottom remains nearly colorless throughout 80 h. Therefore, the Janus separator effectively suppresses the diffusion process of polysulfides due to the strong polysulfide-trapping capability of both the conductive gelatin NF and gelatin/MoS_2 NF as revealed above. We made a comparison of our Janus separator with electrospun nanofabric separators used in Li–S batteries thus far. As displayed in Table S2, most nanofibrous separators demonstrated a monotone function of suppressing the shuttle effect without protecting Li metal. Although there emerges a study[38] on using the nanofibrous separator to protect Li metal, our Janus separator shows a better performance in terms of the longer cycle life. In other words, the Janus separator from our study proposes an innovative separator design to simultaneously addressing the two critical issues of Li–S batteries, that is, shuttle effect and Li dendrite growth.

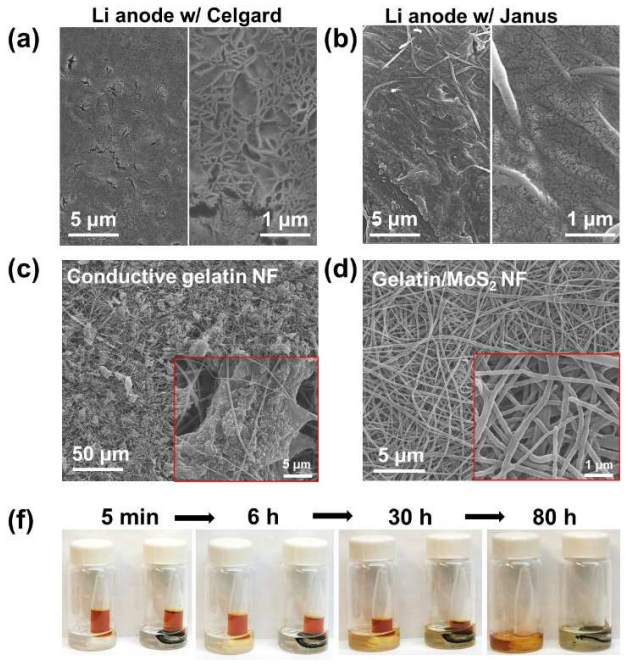

Figure 7. Effects of the Janus separator on Li metal-protecting and polysulfide-trapping. SEM images of Li anodes disassembled from cycled Li–S batteries with (a) pristine Celgard® separator and (b) Janus separator. SEM images of the Janus separator disassembled from cycle Li–S battery consisting of (c) conductive gelatin NF and (d) gelatin/MoS_2 NF. (f) Digital photos showing the diffusion process of polysulfides in a system separated by Celgard® separator (left) and Janus separator (right).

Conclusions

We have reported a protein-based Janus separator incorporating the functions of trapping polysulfides, stabilizing Li^+ deposition and facilitating Li^+ transport. The Janus separator is fabricated by combining a gelatin/MoS_2 nanofabric (NF) for facilitating the Li^+ transport and stabilizing Li^+ deposition, and a conductive gelatin NF for trapping and converting polysulfides. The gelatin/MoS_2 NF shows excellent ionic conductivity of 5.5 mS cm^{-1} and high interfacial affinity with Li metal, benefiting from the nanofibrous structure, Li^+-conducting MoS_2, and surface polarity of gelatin. The conductive gelatin NF shows great effectiveness in adsorbing the polysulfides due to the rich functional groups and high surface area. An integrated electrospinning method is utilized to combine the two NFs and generate the Janus separator with better mechanical properties and structural integrity. Consequently, symmetric Li|Li cells with gelatin/MoS_2 NF separator deliver ultralong cycle life >700 h with a stable and low polarization. The Li–S battery with this Janus separator exhibits excellent rate capacity and remarkable cycle stability (with a low decay rate of 0.063% per cycle at 0.5 A g^{-1} over 500 cycles). This study provides a novel design concept for dual-functional separator and promotes the development of stable, long-life, and safe Li–S batteries.

Experimental Section

Materials

Gelatin protein (from porcine skin, Type A, $M_w = 50000$–100000 g mol^{-1}), molybdenum sulfide (MoS_2), and sulfur were all purchased from Sigma-Aldrich Co. Ltd. Super C45 carbon black (CB)

was purchased from MTI Crop. Carbon nanofibers (CNFs) were purchased from Applied Science, Inc.

Preparation of Janus nanofabrics

Gelatin protein was first dissolved in a solvent mixture of acetic acid/distilled water (AA/DI; 8:2 *w/w*) with a concentration of 0.1 wt%. Then the same amount of MoS_2 powder as gelatin was added and bath sonicated for 1 h to obtain a well-dispersed solution. Subsequently, the dispersion was centrifuged at 9000 rpm for 10 min to isolate the stable MoS_2 dispersion from the unexfoliated MoS_2 sediments. The stable MoS_2 dispersion was mixed with a thick gelatin solution (25 wt% in AA/DI) to improve the viscosity. The concentration of gelatin in the final solution (solution A) was 12.5 wt%. Meanwhile, CNFs were added into a gelatin solution (1 wt% in AA/DI) and the ratio between gelatin and CNF was 1:1. This solution was tip-sonicated for 30 min to disperse the CNFs. Then 25 wt% gelatin solution, CB powders, poly(ethylene oxide) (PEO) solution ($M_w = 1$ million, 3.5 wt% in AA/DI) were added and mixed by mechanical stirring. The weight ratio of each component in the final solution (solution B) was gelatin/CB/CNFs/PEO = 56.2:32.9:5.6:5.3. Solutions A and B were loaded into plastic syringes, respectively, with a stainless-steel nozzle connecting to high DC-voltage and subjected to electrospinning. The electrospinning parameters for the both solutions were 20 kV, 0.5 mL h^{-1} and 150 mm. Solution A was electrospun for a certain time to generate gelatin/MoS_2 nanofabrics. Then solution B was electrospun on the gelatin/MoS_2 nanofabrics to obtain the conductive gelatin nanofabrics. The two different nanofabrics were electrospun in succession on the same collector, which contained an integrated Janus separator.

Preparation of sulfur cathodes

The sulfur cathodes were prepared by mixing 63.8 wt% sulfur powders, 24.1 wt% CB, 2.1 wt% CNFs, and 10 wt% polyvinylidene fluoride (PVDF) in *N*-methylpyrrolidinone (NMP) using a bowl-mill until homogeneity. It is noted that a sulfur/carbon mixture with a sulfur loading of approximately 70.8 wt% was pre-mixed using a bowl-mill (see the thermogravimetric analysis curve in Figure S8) to prepare the sulfur cathode. The slurry was then cast onto carbon-coated aluminum foil and dried at 50 °C overnight. The loading of sulfur active material was controlled to about 1.5 mg cm^{-2}. The liquid electrolyte solution was composed of 1 M lithium bis (trifluoromethanesulfonyl)imide (LiTFSI) dissolved in mixture DOL/DME (1:1 *v/v*), and 2 wt% $LiNO_3$ was added as additive. The electrolyte volume was fixed to be 18 μL for all the cells. The areas of sulfur cathode and lithium anode were 1.27 and 2.01 cm^2, respectively. The thickness of lithium anode was 0.6 mm.

Morphology characterizations

SEM (Quanta 200F) was used to characterize the morphology of the Janus separators and lithium metals as fresh-prepared or after disassembled from cycled batteries. For materials after cycling, they were first extracted from the coin cells in the glovebox and gently rinsed with DOL/DME (1:1 *v/v*) to remove Li salt residue, and then dried in the glovebox for 24 h. SEM, optical microscopy, and TEM (FEI T20) were applied to observe the dispersion of MoS_2. TEM was also used to characterize the morphology of the conductive gelatin nanofabric.

Porosity and electrolyte uptakes characterizations

The porosity of the nanofabric samples was measured via *n*-butanol uptake. Measurement of liquid electrolyte uptake was carried out by dipping the separators in the electrolyte solution. The excess electrolyte remaining on the surface of the samples was removed by wiping softly with a tissue paper. The swelling ratio was defined by the weight ratio of the net liquid uptake to the dried polymer sample [Eq. (1)]:

$$E = [(W_2 - W_1)/W_1] \times 100 \quad (1)$$

where W_1 and W_2 are the mass of the samples before and after dipping in the electrolyte solution, respectively. The measurement of each sample was repeated at least five times for consistency.

Surface properties and conductivity characterizations

The wettability of different nanofabrics was analyzed by contact angle (OCA 25, Dataphysics-Instruments). The ambient ionic conductivity was measured via AC impedance spectroscopy with an electrochemistry workstation (Biologic VSP EC-Lab). The bulk resistance and the ionic conductivity were calculated based on the following Equation (2):

$$\sigma = L/(AR_b) \quad (2)$$

where L is the thickness of the testing samples [cm]; A is the contact area for the sample and electrodes [cm^2], and R_b is the bulk resistance that can be read at the intersection of the x axis [Ω].

Tensile testing

The tensile performance of the integrated Janus separator and the compressed two individual nanofabrics (conductive gelatin and gelatin/MoS_2 nanofabrics) were recorded by dynamic mechanical analyzer (Q800, TA Instruments) by a film tension mode with a strain rate of 3% min^{-1}.

Polysulfide diffusion testing

The Li_2S_6 solution was prepared by adding sulfur and lithium sulfide powders in a 5:1 molar ratio into a solvent mixture of DOL/DME (1:1 *v/v*) and stirred for 24 h under 60 °C. The Li_2S_6 solution and pure DOL/DME were separated by Celgard® and Janus separators, respectively. The color change of the DOL/DME was recorded by digital photos to characterize the polysulfide diffusion.

Electrochemical performance testing

EIS was used to characterize the impedance of the cells via an electrochemical workstation (Biologic VSP EC-Lab) over a frequency range of 0.01–10^6 Hz. The galvanostatic charge/discharge measurements were monitored using the LANHE battery testing system (CT2001A, Wuhan LAND electronics Co., China) with a voltage range of 1.8–2.8 V.

Acknowledgements

This work was supported by NSF CBET 1929236. Dr. Min Chen was sponsored by the China Scholarship Council for her visit at

Washington State University. The authors would like to gratefully acknowledge the support on microscopy characterizations from the Franceschi Microscopy & Imaging Center at Washington State University.

Conflict of Interest

The authors declare no conflict of interest.

Keywords: electrochemistry · electrospinning · Janus separator · Li–S batteries · shuttle effect

[1] a) X. Luo, X. Lu, X. Chen, Y. Chen, C. Yu, D. Su, G. Wang, L. Cui, *J. Energy Chem.* **2020**, *50*, 63–72; b) H. Ye, J. Y. Lee, *Small Methods* **2020**, *4*, 1900864.
[2] a) Y. Gao, Q. Guo, Q. Zhang, Y. Cui, Z. Zheng, *Adv. Energy Mater.* **2020**, 2002580; b) L. Zhang, Y. Wang, Z. Niu, J. Chen, *Carbon* **2019**, *141*, 400–416.
[3] a) D. Lin, Y. Liu, Y. Cui, *Nat. Nanotechnol.* **2017**, *12*, 194; b) S. J. Zhang, Z. G. Gao, W. W. Wang, Y. Q. Lu, Y. P. Deng, J. H. You, J. T. Li, Y. Zhou, L. Huang, X. D. Zhou, *Small* **2018**, *14*, 1801054.
[4] a) P. Yu, L.-X. Feng, D.-C. Ma, X.-R. Sun, J.-K. Pei, X.-J. Zha, R.-Y. Bao, Y. Wang, M.-B. Yang, Z.-P. Guo, W. Yang, *Adv. Funct. Mater.* **2021**, 2008652; b) S. H. Chung, C. H. Chang, A. Manthiram, *Energy Environ. Sci.* **2016**, *9*, 3188–3200.
[5] a) B. Jin, L. Yang, J. Zhang, Y. Cai, J. Zhu, J. Lu, Y. Hou, Q. He, H. Xing, X. Zhan, F. Chen, Q. Zhang, *Adv. Energy Mater.* **2019**, *9*, 1902938; b) X. Fu, L. Scudiero, W.-H. Zhong, *J. Mater. Chem. A* **2019**, *7*, 1835–1848.
[6] a) M. Rao, X. Geng, X. Li, S. Hu, W. Li, *J. Power Sources* **2012**, *212*, 179–185; b) E. Temeche, X. Zhang, R. M. Laine, *ACS Appl. Mater. Interfaces* **2020**, *12*, 30353–30364.
[7] a) M. Chen, X. Fu, N. D. Taylor, Z. Chen, W.-H. Zhong, *ACS Sustainable Chem. Eng.* **2019**, *7*, 15267–15277; b) S. Tu, X. Chen, X. Zhao, M. Cheng, P. Xiong, Y. He, Q. Zhang, Y. Xu, *Adv. Mater.* **2018**, *30*, 1804581.
[8] a) S. Zhang, K. Ueno, K. Dokko, M. Watanabe, *Adv. Energy Mater.* **2015**, *5*, 1500117; b) F. Ding, W. Xu, G. L. Graff, J. Zhang, M. L. Sushko, X. Chen, Y. Shao, M. H. Engelhard, Z. Nie, J. Xiao, *J. Am. Chem. Soc.* **2013**, *135*, 4450–4456.
[9] a) J. Liang, Q. Chen, X. Liao, P. Yao, B. Zhu, G. Lv, X. Wang, X. Chen, J. Zhu, *Angew. Chem. Int. Ed.* **2020**, *59*, 6561–6566; *Angew. Chem.* **2020**, *132*, 6623–6628; b) Y. Liu, S. Xiong, J. Wang, X. Jiao, S. Li, C. Zhang, Z. Song, J. Song, *Energy Storage Mater.* **2019**, *19*, 24–30.
[10] a) G. Ma, Z. Wen, M. Wu, C. Shen, Q. Wang, J. Jin, X. Wu, *Chem. Commun.* **2014**, *50*, 14209–14212; b) B. Zhu, Y. Jin, X. Hu, Q. Zheng, S. Zhang, Q. Wang, J. Zhu, *Adv. Mater.* **2017**, *29*, 1603755.
[11] a) C.-P. Yang, Y.-X. Yin, S.-F. Zhang, N.-W. Li, Y.-G. Guo, *Nat. Commun.* **2015**, *6*, 8058; b) Y. Liu, D. Lin, Z. Liang, J. Zhao, K. Yan, Y. Cui, *Nat. Commun.* **2016**, *7*, 10992.
[12] a) W. Kong, L. Yan, Y. Luo, D. Wang, K. Jiang, Q. Li, S. Fan, J. Wang, *Adv. Funct. Mater.* **2017**, *27*, 1606663; b) J. Q. Huang, Z. L. Xu, S. Abouali, M. A. Garakani, J. K. Kim, *Carbon* **2016**, *99*, 624–632; c) S. H. Chung, A. Manthiram, *Adv. Funct. Mater.* **2014**, *24*, 5299–5306.
[13] a) J.-L. Yang, S.-X. Zhao, Y.-M. Lu, X.-T. Zeng, W. Lv, G.-Z. Cao, *Nano Energy* **2020**, *68*, 104356; b) Y. Zang, F. Pei, J. Huang, Z. Fu, G. Xu, X. Fang, *Adv. Energy Mater.* **2018**, *8*, 1802052; c) X. Fu, Y. Wang, L. Scudiero, W.-H. Zhong, *Energy Storage Mater.* **2018**, *15*, 447–457.
[14] P. Wang, J. Bao, K. Lv, N. Zhang, Z. Chang, P. He, H. Zhou, *ACS Appl. Mater. Interfaces* **2019**, *11*, 35788–35795.
[15] S. S. Zhang, X. Fan, C. Wang, *J. Mater. Chem. A* **2018**, *6*, 10755–10760.
[16] H. Lee, X. Ren, C. Niu, L. Yu, M. H. Engelhard, I. Cho, M.-H. Ryou, H. S. Jin, H.-T. Kim, J. Liu, W. Xu, J.-G. Zhang, *Adv. Funct. Mater.* **2017**, *27*, 1704391.
[17] a) X. Li, J. Tao, D. Hu, M. H. Engelhard, W. Zhao, J.-G. Zhang, W. Xu, *J. Mater. Chem. A* **2018**, *6*, 5006–5015; b) W. Liu, D. Lin, A. Pei, Y. Cui, *J. Am. Chem. Soc.* **2016**, *138*, 15443–15450.
[18] C. Ma, Y. Feng, X. Liu, Y. Yang, L. Zhou, L. Chen, C. Yan, W. Wei, *Energy Storage Mater.* **2020**, *32*, 46–54.
[19] a) Y. Li, W. Wang, X. Liu, E. Mao, M. Wang, G. Li, L. Fu, Z. Li, A. Y. S. Eng, Z. W. Seh, Y. Sun, *Energy Storage Mater.* **2019**, *23*, 261–268; b) K. Xie, K. Yuan, K. Zhang, C. Shen, W. Lv, X. Liu, J.-G. Wang, B. Wei, *ACS Appl. Mater. Interfaces* **2017**, *9*, 4605–4613.
[20] M. Chen, C. Li, X. Fu, W. Wei, X. Fan, A. Hattori, Z. Chen, J. Liu, W.-H. Zhong, *Adv. Energy Mater.* **2020**, *10*, 1903642.
[21] X. Fu, Y. Jewel, Y. Wang, J. Liu, W. H. Zhong, *J. Phys. Chem. Lett.* **2016**, *7*, 4304.
[22] M. Chen, Z. Chen, X. Fu, W.-H. Zhong, *J. Mater. Chem. A* **2020**, *8*, 7377–7389.
[23] M. Lian, J. Fan, Z. Shi, S. Zhang, H. Li, J. Yin, *Carbon* **2015**, *89*, 279–289.
[24] Cha, Eunho, Patel, D. Mumukshu, Park, Juhong, Hwang, Jeongwoon, Prasad, *Nat. Nanotechnol.* **2018**, *13*, 337–344..
[25] a) Y. Jewel, T. Liu, A. Eyler, W. H. Zhong, J. Liu, *J. Phys. Chem. C* **2015**, *119*; b) T. Liu, Y. Wang, A. Eyler, Y. C. Chang, W. H. Zhong, *eXPRESS Polym. Lett.* **2015**, *9*, 686–694.
[26] J. Y. Ji, B. Lively, W. H. Zhong, *Mater. Express* **2012**, *2*, 76–82.
[27] Y. Zhang, C. Y. Wu, S. W. Guo, J. Y. Zhang, *Nanotechnol. Rev.* **2013**, *2*, 27–45.
[28] M. Chen, X. Fu, Z. Chen, J. Liu, W.-H. Zhong, *Adv. Funct. Mater.* **2021**, *31*, 2006744.
[29] Z. A. Ghazi, X. He, A. M. Khattak, N. A. Khan, B. Liang, A. Iqbal, J. Wang, H. Sin, L. Li, Z. Tang, *Adv. Mater.* **2017**, *29*, 1606817.
[30] G. Bieker, M. Winter, P. Bieker, *Phys. Chem. Chem. Phys.* **2015**, *17*, 8670–8679.
[31] C. Wang, A. Wang, L. Ren, X. Guan, D. Wang, A. Dong, C. Zhang, G. Li, J. Luo, *Adv. Funct. Mater.* **2019**, *29*, 1905940.
[32] a) J. Zhao, J. Zhang, P. Hu, J. Ma, X. Wang, L. Yue, G. Xu, B. Qin, Z. Liu, X. Zhou, G. Cui, *Electrochim. Acta* **2016**, *188*, 23–30; b) C.-H. Chang, S.-H. Chung, A. Manthiram, *Adv. Sustainable Syst.* **2017**, *1*, 1600034; c) T. Wang, Y. Li, J. Zhang, K. Yan, P. Jaumaux, J. Yang, C. Wang, D. Shanmukaraj, B. Sun, M. Armand, Y. Cui, G. Wang, *Nat. Commun.* **2020**, *11*, 5429; d) C. Ding, X. Fu, H. Li, J. Yang, J.-L. Lan, Y. Yu, W.-H. Zhong, X. Yang, *Adv. Funct. Mater.* **2019**, *29*, 1904547; e) B.-C. Yu, K. Park, J.-H. Jang, J. B. Goodenough, *ACS Energy Lett.* **2016**, *1*, 633–637.
[33] a) L. Kong, X. Fu, S. Qi, D. Wu, Y. Wang, W.-H. Zhong, *Electrochim. Acta* **2019**, *318*, 220–227; b) D. Zhang, A. Dai, M. Wu, K. Shen, T. Xiao, G. Hou, J. Lu, Y. Tang, *ACS Energy Lett.* **2020**, *5*, 180–186.
[34] N. A. Canas, K. Hirose, B. Pascucci, N. Wagner, K. A. Friedrich, R. Hiesgen, *Electrochim. Acta* **2013**, *97*, 42–51.
[35] H. Wang, Q. Zhang, H. Yao, Z. Liang, H.-W. Lee, P.-C. Hsu, G. Zheng, Y. Cui, *Nano Lett.* **2014**, *14*, 7138–7144.
[36] X. Fu, C. Li, Y. Wang, L. Scudiero, J. Liu, W. H. Zhong, *J. Phys. Chem. Lett.* **2018**, *9*, 2450–2459.
[37] S. Zhang, *Energies* **2012**, *5*, 5190–5197.
[38] C. Zhou, Q. He, Z. Li, J. Meng, X. Hong, Y. Li, Y. Zhao, X. Xu, L. Mai, *Chem. Eng. J.* **2020**, *395*, 124979.

Manuscript received: March 19, 2021
Accepted manuscript online: March 22, 2021
Version of record online: April 21, 2021